Check for updates

Nonradiative Recombination Dominates Voltage Losses in $Cu(In,Ga)Se_2$ Solar Cells Fabricated using Different Methods

Alexandra M. Bothwell, Jake Wands, Michael F. Miller, Ana Kanevce, Stefan Paetel, Polyxeni Tsoulka, Thomas Lepetit, Nicolas Barreau, Nicholas Valdes, William Shafarman, Angus Rockett, Aaron R. Arehart, and Darius Kuciauskas*

Voltage losses reduce the photovoltaic conversion efficiency of thin-film solar cells and are a primary efficiency limitation in $Cu(In,Ga)Se_2$. Herein, voltage loss analysis of $Cu(In,Ga)Se_2$ solar cells fabricated at three institutions with variation in process, bandgap, absorber structure, postdeposition treatment (PDT), and efficiency is presented. Nonradiative voltage losses due to Shockley–Read–Hall charge carrier recombination dominate and constitute >75% of the total compared to <25% from radiative voltage losses. The radiative voltage loss results from nonideal absorption and carriers in band tails that stem from local composition-driven potential fluctuations. It is shown that significant bulk lifetime improvements are achieved for all alkali PDT processed absorbers, chiefly associated with reductions in nonradiative recombination. Primary voltage loss contributions (radiative and nonradiative) change little across fabrication processes, but variation in submechanisms (bulk lifetime, net acceptor concentration, and interface recombination) differentiate nonradiative loss pathways in this series of solar cells.

1. Introduction

$Cu(In,Ga)Se_2$ (CIGS)-based thin film solar cells hold significant promise due to the tunable, direct bandgap, high absorption coefficient, thin layers, flexible and rigid substrate applications, processing options, and consistent efficiency increases.[1–3] Photovoltaic conversion efficiencies have reached 23.4% in small-area CIGS solar cells,[4] and significant improvements have originated from absorber composition changes and heavy alkali postdeposition treatments (PDTs).[5–13]

The absorber energy gap and electron affinity can be controlled by the Ga/(Ga+In) (GGI) ratio, which offers two benefits. First, increases in GGI widen the absorber bandgap which raises the maximum achievable open circuit voltage (V_{OC}) and efficiency of the device.[14] Second, GGI grading is used to create a "notched" graded bandgap in which the bandgap is increased at both the front and rear portions of the absorber, and a bandgap minimum is maintained in the front half of the absorber.[6] The front-side bandgap increase reduces front interface hole recombination and back-side grading reduces back interface electron recombination such that V_{OC} improvements up to 100 mV are achievable with a change in GGI ≈ 0.5.[15,16] However, voltage losses increase for GGI > 0.4 in the minimum bandgap region such that efficiency improvements are limited.[17–19] This can be mitigated in part through silver-alloyed ACIGS devices ($(Ag,Cu)(In,Ga)Se_2$), which

A. M. Bothwell, D. Kuciauskas
Materials, Chemical, and Computational Science
National Renewable Energy Laboratory
Golden, CO 80401, USA
E-mail: a.bothwell3@gmail.com

J. Wands, A. Rockett
Metallurgical and Materials Engineering
Colorado School of Mines
Golden, CO 80401, USA

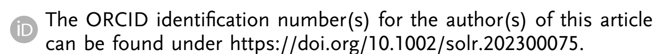
The ORCID identification number(s) for the author(s) of this article can be found under https://doi.org/10.1002/solr.202300075.

© 2023 The Authors. Solar RRL published by Wiley-VCH GmbH. This is an open access article under the terms of the Creative Commons Attribution-NonCommercial-NoDerivs License, which permits use and distribution in any medium, provided the original work is properly cited, the use is non-commercial and no modifications or adaptations are made.

DOI: 10.1002/solr.202300075

M. F. Miller, A. R. Arehart
The Ohio State University
Columbus, OH 43210, USA

A. Kanevce, S. Paetel
Zentrum für Sonnenenergie-und Wasserstoff-Forschung
70563 Stuttgart, Germany

P. Tsoulka, T. Lepetit, N. Barreau
Nantes Université
CNRS
Institut des Matériaux de Nantes Jean Rouxel
IMN
F-44000 Nantes, France

N. Valdes, W. Shafarman
Institute of Energy Conversion
University of Delaware
Newark, DE 19716, USA

have demonstrated higher V_{OC} and efficiency with a wider bandgap.[18,20–22]

Heavy alkali PDTs, including CsF, RbF, and KF, have led to notable efficiency increases, in large part due to improved V_{OC}.[8–13] This has been related to improvements in the absorber bulk, specifically the accumulation of heavy alkalis which leads to the reduction of charged defects at grain boundaries.[8]

Voltage losses have been discussed in the literature in the context of GGI and heavy alkalis in CIGS devices; however, most studies have investigated voltage losses in a limited set of device structures and primarily through the lens of external radiative efficiency, Urbach energies, optical losses, or defects.[8,23,24] Studies that analyzed a diverse set of devices did not include detailed voltage loss assessment.[2] As summarized by Kirchartz and Rau,[25] a majority of the losses in CIGS are nonradiative recombination losses.

In this work, we characterize voltage losses and mechanisms across devices fabricated at three institutions with variations in bandgap (1.0–1.19 eV), absorber structure (Ga inclusion, Ag-alloying), PDT (RbF and KF treatments), and efficiency (10.4–17.5%). Across all devices, voltage losses were dominated by nonradiative recombination—which contributed >75% of the total—compared to <25% contribution from radiative voltage loss. Ga inclusion reduced voltage losses while Ag-alloying did not have a consistent effect. Generally, PDTs decreased voltage loss through reduced nonradiative recombination, specifically by increased minority carrier lifetime. In contrast, PDTs did not demonstrate a consistent effect on radiative voltage loss. Therefore, further reductions in radiative losses will likely require fabrication advances beyond PDTs. This work emphasizes that the dominant voltage loss mechanism in CIGS devices, nonradiative recombination, and the bulk lifetime-induced improvement after PDT are fabrication agnostic.

2. Results

2.1. Device Performance, Bandgaps, and Radiative Voltage

V_{OC} is fundamentally limited by the device bandgap (E_g),[26] and the difference between E_g and measured V_{OC} is often described as the voltage deficit. V_{OC} values were extracted from current density–voltage (J–V) measurements, as shown in **Figure 1**a–c, and all performance parameters are tabulated in **Table 1**. RbF-based PDTs increased V_{OC} across all manufacturers and absorber structures. V_{OC} reduction in the ACIS device compared to CIS device (devices C) regardless of PDT, as well as reported success of Ag-alloying in CIGS architectures[20–22] may suggest that Ag-alloying may be better suited for Ga-containing absorbers. Devices without Ga (CIS and ACIS) demonstrated the lowest device efficiencies and V_{OC}s, and we will show that the difference in voltage between Ga-containing and non-Ga devices is due to more than bandgap.

External quantum efficiency (EQE) spectra, as shown in Figure 1d–f, were used to quantify E_g in all devices according to the method outlined by Rau et al.[27] It submits that the shape of the EQE(E) derivative at the band edge is described by a distribution of bandgap energies ($P(E_g)$) and is given by

$$P(E_g) = \frac{d}{dE}\text{EQE}(E) \quad (1)$$

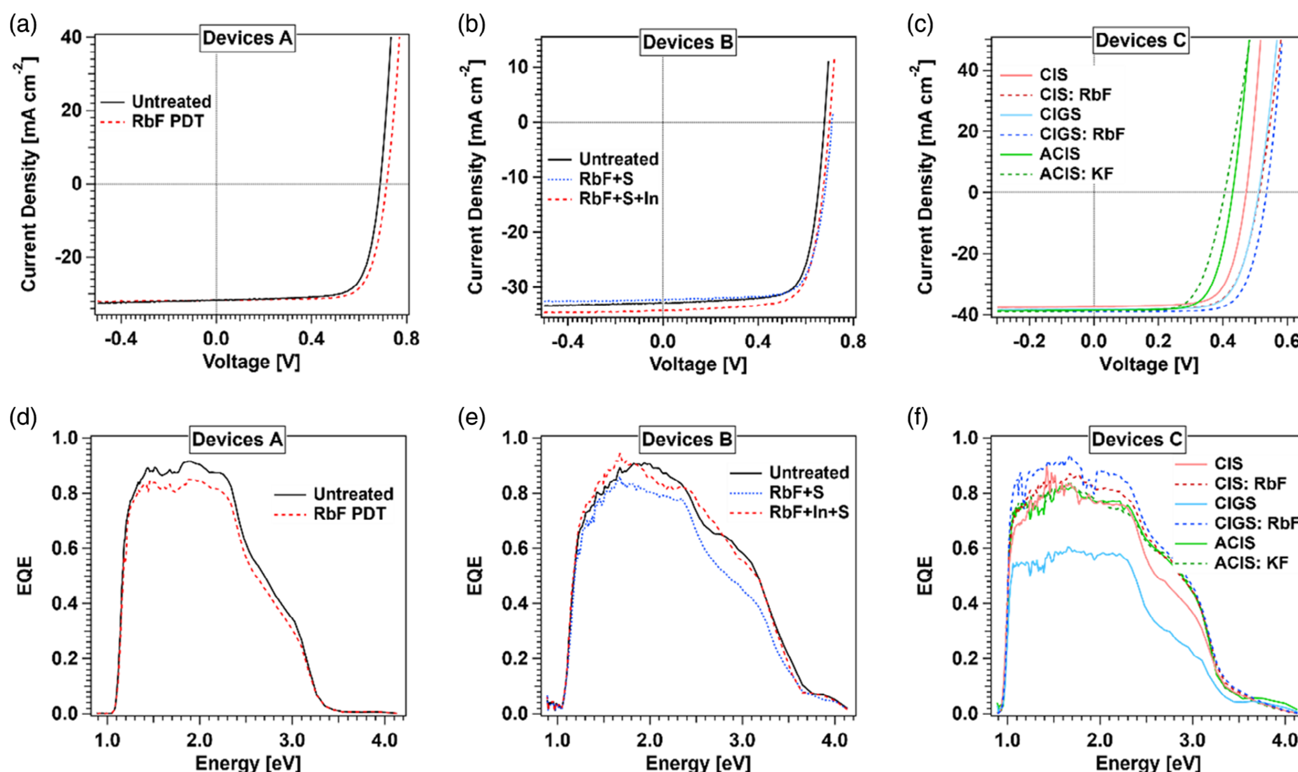

Figure 1. J–V curves of a) A, b) B, and c) C devices. EQE spectra of d) A, e) B, and f) C devices.

© 2023 The Authors. Solar RRL published by Wiley-VCH GmbH

2367198x, 2023, 11, Downloaded from https://onlinelibrary.wiley.com/doi/10.1002/solr.202300075 by National Renewable Energy Lab, Wiley Online Library on [08/06/2023]. See the Terms and Conditions (https://onlinelibrary.wiley.com/terms-and-conditions) on Wiley Online Library for rules of use; OA articles are governed by the applicable Creative Commons License

2367198x, 2023, 11, Downloaded from https://onlinelibrary.wiley.com/doi/10.1002/solr.202300075 by National Renewable Energy Lab, Wiley Online Library on [08/06/2023]. See the Terms and Conditions (https://onlinelibrary.wiley.com/terms-and-conditions) on Wiley Online Library for rules of use; OA articles are governed by the applicable Creative Commons License

Table 1. Device structures and performance parameters.

Device	Absorber	PDT	E_g [eV]	V_{OC} [mV]	J_{SC} [mA cm^{-2}]	FF [%]	Eff. [%]
A	CIGS	None	1.15	688	31.7	74.6	16.3
		RbF	1.16	716	31.7	75.7	17.2
B	CIGS	None	1.14	678	32.8	74.3	16.5
		RbF + S	1.16	712	32.2	74.0	17.0
		RbF + In+S	1.14	700	34.2	73.2	17.5
C	CIS	None	1.00	472	37.3	71.9	12.7
		RbF	1.00	513	38.3	70.6	13.9
	CIGS	None	1.00	511	38.2	71.7	14.0
		RbF	1.00	535	39.0	73.4	15.3
	ACIS	None	1.00	430	38.5	70.5	11.7
		KF	1.00	406	38.7	66.0	10.4

The bandgap is then determined by

$$E_g = \frac{\int_a^b E \cdot P(E_g) dE}{\int_a^b P(E_g) dE} \quad (2)$$

where a and b are the energies at which $P(E_g)$ is half that of its maximum, $P(a) = P(b) = \max(P(E_g))/2$. The calculated bandgaps are given in Table 1.

Voltage loss is distinct from the voltage deficit, E_g–V_{OC}, because it quantifies the voltage difference in terms of the Shockley–Queisser (SQ) voltage, $V_{OC,SQ}$, and the thermodynamic voltage limit.[26,28] This description is especially appropriate for comparisons between devices with various bandgaps, typified here. Therefore, voltage loss in this work is taken to be $V_{OC,SQ}$–V_{OC}, also referred to as the V_{OC} voltage change. This difference combines radiative and nonradiative losses and contact selectivity losses although contact selectivity losses are not considered here. Radiative losses are characterized by radiative voltage, $V_{OC,rad}$, calculated by[29]

$$V_{OC,rad} = \frac{kT}{q} \ln\left(\frac{J_{SC}}{J_{0,rad}} + 1\right) \quad (3)$$

where q is the elementary charge, k is Boltzmann's constant, and T is temperature. The short circuit current density is

$$J_{SC} = q \int_0^\infty \mathrm{EQE}(E) \cdot \phi_{sun}(E) dE \quad (4)$$

where $\phi_{sun}(E)$ is the AM1.5G solar spectrum photon flux. The radiative saturation current density, $J_{0,rad}$ is given by[25]

$$J_{0,rad} = q \int_0^\infty \mathrm{EQE}(E) \cdot \phi_{BB}(E) dE \quad (5)$$

where $\phi_{BB}(E)$ is the blackbody spectrum photon flux $\phi_{BB} = \frac{2\pi}{c^2 h^3} \frac{E^2}{\left[\exp\left(\frac{E}{kT}\right) - 1\right]}$. h is Planck's constant and c is photon velocity in vacuum. $V_{OC,rad}$ values, calculated from $\mathrm{EQE}(E)$ and Equation (3)–(5), are given in **Figure 2**a.

In the SQ-limit, complete absorption of photons with energy greater than or equal to the bandgap is assumed, i.e., $\mathrm{EQE}(E) = a(E) = 1$ for $E \geq E_g$ and $= 0$ for $E < E_g$, where $a(E)$ is energy-dependent absorptivity. $V_{OC,SQ}$ values calculated using Equation (3)–(5) where the Heaviside step function is utilized for $a(E)$, are given in Figure 2a.

Using the approach outlined above, each device is characterized by bandgap E_g, SQ voltage $V_{OC,SQ}$, radiative voltage $V_{OC,rad}$ (Equation (3)), and device voltage V_{OC}. The total voltage losses $V_{OC,SQ}$–V_{OC} are shown in Figure 2b. This difference includes voltage reduction due to subbandgap states (radiative losses $V_{OC,SQ}$–$V_{OC,rad}$) and nonradiative Shockley–Read–Hall (SRH) recombination ($V_{OC,rad}$–V_{OC}), both also given in Figure 2b. Auger recombination is not considered because it is an insignificant recombination mechanism at the typical injection levels used in this work.[30]

Figure 2c provides the percentage loss contribution from radiative and nonradiative voltage losses. Nonradiative SRH recombination was the dominant voltage loss mechanism in all devices regardless of architecture, bandgap, PDT, or performance, generating >75% of the total voltage loss. Concomitantly, nonradiative losses contributed <25% to the total. The nonradiative voltage changes are discussed in detail in Section 2.2.

Radiative voltage losses stem from incomplete absorption and donor and acceptor distribution inhomogeneities at the nanometer scale (fluctuations). Incomplete absorption is particularly relevant in thin-film solar cells such as CIGS with absorbers ≈2 μm and bandgap grading which leads to a nonideal absorption edge. Fluctuations occur in many compound materials such as CIGS. Bandgap fluctuations describe spatial variations in the fundamental bandgap caused by compositional variations, stress, and stoichiometry. Electrostatic potential fluctuations describe distortions in the band structure caused by a distribution of charged states from structural defects, dopants, and impurities.[31] In the CIGS devices analyzed here, radiative voltage losses ranged from 23 to 52 mV, in agreement with the radiative loss range predicted by Wolter et al.[24] PDTs did not exhibit a consistent effect on radiative loss: devices A and B demonstrated increased radiative losses after PDT while devices C exhibited lower losses.

2.2. Nonradiative Voltage Losses

Nonradiative SRH recombination originates from a combination of mechanisms. The relevant material and device characteristics which affect SRH recombination include minority carrier lifetime in the absorber (τ_{bulk}), net acceptor concentration (N_A), back and front interface recombination velocities, and band bending. We analyze the SRH recombination losses given in Figure 2b to understand their origins. Time-resolved photoluminescence (TRPL) and capacitance–voltage (C–V) data are utilized for τ_{bulk} and N_A determination, respectively, to estimate minority and majority carrier densities in these solar cells.

Figure 3a–c shows low-injection TRPL data for devices A, B, and C. Effective lifetimes, τ_{eff}, increased significantly (**Table 2**) in all PDT devices compared to their untreated counterparts. As is commonly used for CIGS, τ_{eff} values were determined by single exponential fits to the TRPL decay tail, shown by gray fit lines in Figure 3a–c. To quantify changes in τ_{bulk}, voltage-biased TRPL measurements were performed at low injection according to

© 2023 The Authors. Solar RRL published by Wiley-VCH GmbH

2367198x, 2023, 11, Downloaded from https://onlinelibrary.wiley.com/doi/10.1002/solr.202300075 by National Renewable Energy Lab, Wiley Online Library on [08/06/2023]. See the Terms and Conditions (https://onlinelibrary.wiley.com/terms-and-conditions) on Wiley Online Library for rules of use; OA articles are governed by the applicable Creative Commons License

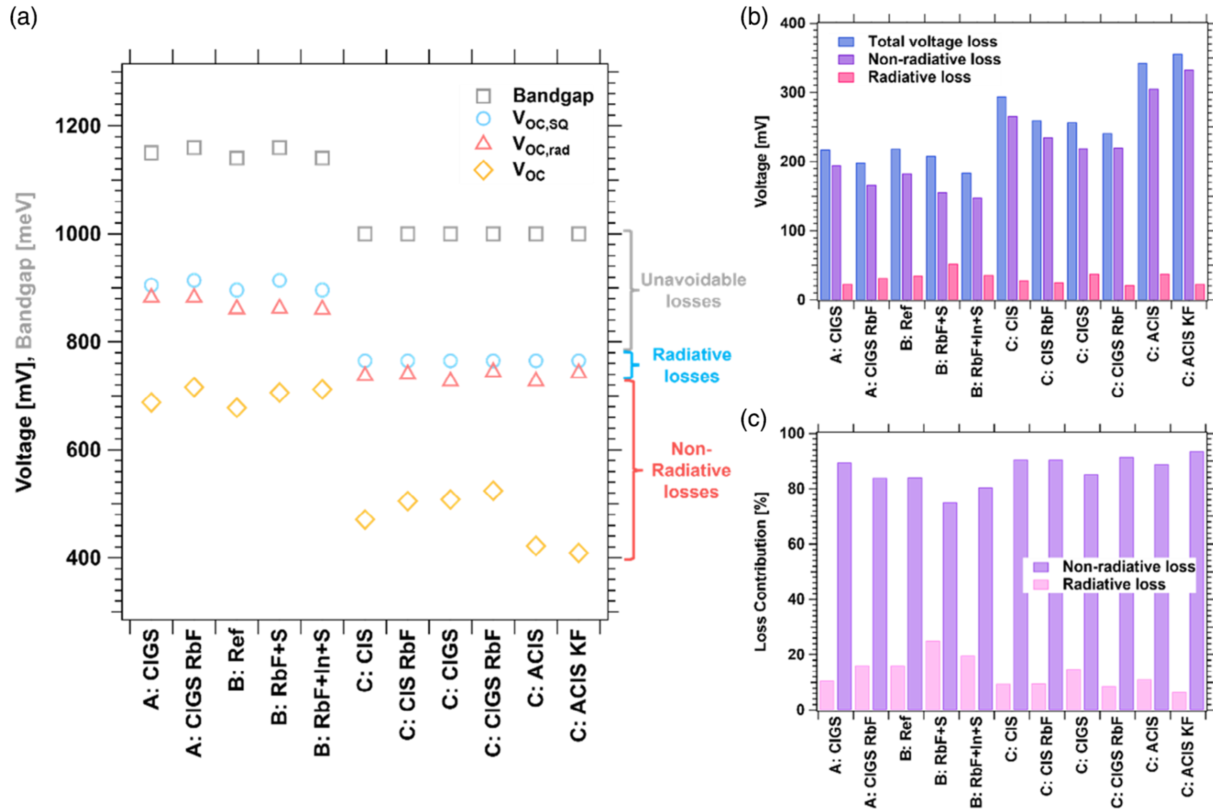

Figure 2. a) Bandgap (E_g), SQ voltages, radiative voltages, and device voltages for solar cells in this study. Gray, blue, and red brackets identify unavoidable voltage losses (E_g–$V_{OC,SQ}$), radiative losses ($V_{OC,SQ}$–$V_{OC,rad}$), and nonradiative, SRH recombination losses ($V_{OC,rad}$–V_{OC}), respectively. b) Total voltage losses compared to radiative and nonradiative losses and c) loss contribution percentages show that nonradiative SRH recombination was the dominant loss category in all devices.

the method by Maiberg et al.[32] This method analyzes changes in τ_{eff} with applied voltage bias (V)

$$\frac{1}{\tau_{eff}} = \frac{1}{\tau_{b,n}} + \frac{1}{\tau_{b,p}} + \frac{\mu_n + \mu_p}{4V_T d^2}(V_{bi} - V)^2 \quad (6)$$

$\tau_{b,n}$ and $\tau_{b,p}$ are minority and majority bulk lifetimes, respectively (corresponding to electrons and holes in CIGS), μ_n, and μ_p are minority and majority mobilities, V_T is the thermal voltage, (≈25 mV at room temperature), d is absorber thickness, and V_{bi} is built-in voltage. Changes in TRPL decay rates with voltage bias are induced by a change in the electric field, interface recombination, and electron extraction into the TCO at different voltage biases. Voltage-biased TRPL decay lifetimes (τ_{eff}^{-1} vs applied voltage) and three-order polynomial fits to Equation (6) were used to determine minority carrier lifetimes. Examples are provided in the Supporting Information section. A few devices exhibited voltage-independent decays which can be caused by field effects, low doping, or nonstandard transport mechanisms like trapping.[32,33] In these cases, τ_{eff} measured with forward-bias was used to approximate τ_{bulk}.

τ_{bulk} values extracted using this approach are listed in Table 2. Significant increases after PDT were observed for all devices. Increased minority carrier lifetime is primarily attributed to reduced nonradiative recombination because $\tau_{bulk} = 7$–224 ns is well below the radiative lifetime, $\tau_R \approx 1000$ ns ($\tau_R = 1/(BN_A)$ where $B = 1.67 \times 10^{-10}$ cm^3 s^{-1} [34] and N_A values are listed in Table 2 and discussed below. The τ_{bulk}-associated voltage increase can be estimated by[35]

$$\Delta V_{OC,\,bulk} = \frac{kT}{q}\ln\left(\frac{\tau_{bulk,PDT}}{\tau_{bulk,untreated}}\right) \quad (7)$$

Voltage improvements due to increased bulk lifetime after PDT ($\Delta V_{OC,bulk}$) ranged from 30 to 71 mV, listed in Table 2. Given that recombination center concentration (N_T) is linear with the recombination rate, $\tau_{bulk} = \sigma v_{th} N_T$, where σ is capture cross section and v_{th} is thermal velocity, which has been observed in similar samples,[21,22] the improvements to τ_{bulk} in these devices likely originate from a reduction in mid-gap defect concentration.

Next, we consider doping changes after PDT and their effect on the voltage. Voltage changes $\Delta V_{OC,NA}$ due to change in N_A can be similarly quantified by application of Equation (7), with $N_{A,PDT}$ in the numerator and $N_{A,untreated}$ in the denominator. Figure 3d–f shows the carrier concentration profiles for each device, and Table 2 provides N_A values from the zero-voltage point and the voltage changes $\Delta V_{OC,NA}$ associated with PDTs.

Unlike voltage improvements from increased τ_{bulk}, N_A values generally decreased after PDT and induced voltage loss. This

© 2023 The Authors. Solar RRL published by Wiley-VCH GmbH

2367198x, 2023, 11, Downloaded from https://onlinelibrary.wiley.com/doi/10.1002/solr.202300075 by National Renewable Energy Lab, Wiley Online Library on [08/06/2023]. See the Terms and Conditions (https://onlinelibrary.wiley.com/terms-and-conditions) on Wiley Online Library for rules of use; OA articles are governed by the applicable Creative Commons License

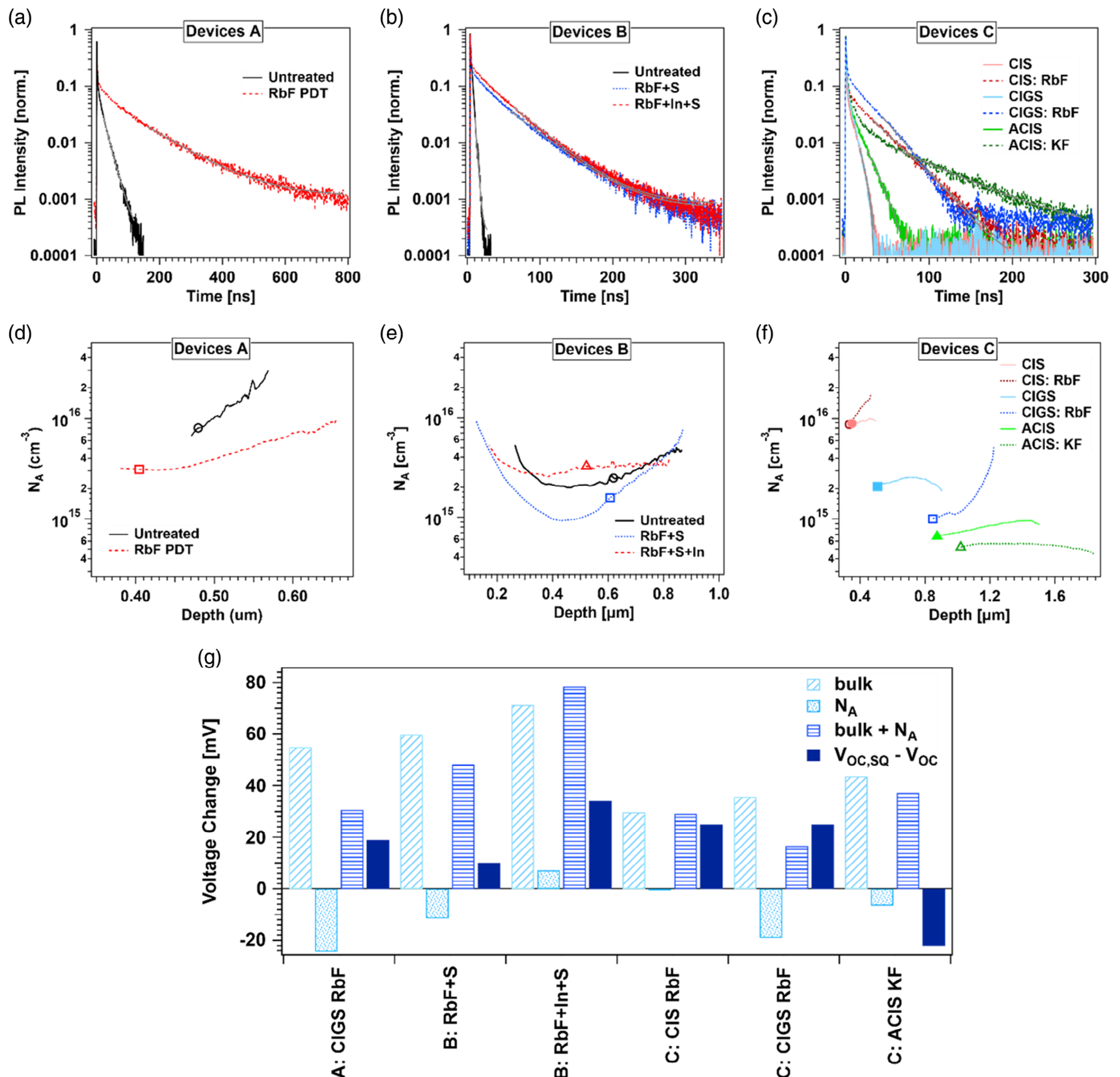

Figure 3. TRPL decays for devices a) A, b) B, and c) C. Gray lines show the region of fit. *C–V* profiles for devices d) A, e) B, and f) C. Symbols indicate the 0 V point from which N_A was extracted. Bar graphs in g) indicate voltage changes after PDT due to bulk lifetime $\Delta V_{OC,bulk}$ (light blue) and absorber doping $\Delta V_{OC,NA}$ (middle blue, dotted). The combined $\Delta V_{OC,bulk} + \Delta V_{OC,NA}$ (royal blue, lines) is compared with the V_{OC} voltage change due to PDT $\Delta(V_{OC,SQ}–V_{OC})$ (dark blue, solid) (compare to Figure 2b).

agrees with variable changes in N_A after PDT, reported in the literature.[12,13,36–39] However, absolute $\Delta V_{OC,NA}$ values were smaller than $\Delta V_{OC,bulk}$ such that a net positive voltage change due to these two mechanisms is expected in PDT devices.

Voltage changes $\Delta V_{OC,bulk}$, $\Delta V_{OC,NA}$, their combination ($\Delta V_{OC,bulk} + \Delta V_{OC,NA}$), and the V_{OC} voltage change loss after PDT, $\Delta(V_{OC,SQ}–V_{OC})$, are given in Figure 3g. Comparison between the latter two categories reveals whether bulk lifetime and carrier density constitute the dominant mechanisms for voltage change after PDT. For almost all devices the anticipated voltage improvement via $\tau_{bulk} + N_A$ was larger than was actually achieved, $\Delta(V_{OC,SQ}$-$V_{OC})$.

CIS and CIGS devices A and C demonstrated that the voltage change after RbF PDT was dictated primarily by τ_{bulk} and N_A: only 12, 4, and 8 mV respectively were not accounted for with these two mechanisms. The remaining difference could be attributed to interface recombination, including back contact/band bending.

Alternatively, τ_{bulk} and N_A were not the only significant mechanisms of voltage change in the other devices. A range of voltage

© 2023 The Authors. Solar RRL published by Wiley-VCH GmbH

2367198x, 2023, 11, Downloaded from https://onlinelibrary.wiley.com/doi/10.1002/solr.202300075 by National Renewable Energy Lab, Wiley Online Library on [08/06/2023]. See the Terms and Conditions (https://onlinelibrary.wiley.com/terms-and-conditions) on Wiley Online Library for rules of use; OA articles are governed by the applicable Creative Commons License

Table 2. PDT-associated nonradiative voltage losses: V_{OC} voltage change ($\Delta V_{OC,SQ}$–V_{OC}), minority carrier lifetimes and associated voltage losses ($\Delta V_{OC,bulk}$), and carrier concentrations and associated voltage losses ($\Delta V_{OC,NA}$).

Device	Absorber	PDT	$\Delta V_{OC,SQ}$–V_{OC} [mV]	τ_{eff} [ns]	τ_{bulk} [ns]	$\Delta V_{OC,bulk}$ [mV]	N_A [cm^{-3}]	$\Delta V_{OC,NA}$ [mV]
A	CIGS	none	19	19	19	55	8.0×10^{15}	−24
		RbF		125	161		3.1×10^{15}	
B	CIGS	none		3	14		2.5×10^{15}	
		RbF + S	27	43	143	60	1.6×10^{15}	−11
		RbF + In+S	35	41	224	71	3.3×10^{15}	7
C	CIS	none	25	8	22	30	8.9×10^{15}	−1
		RbF		30	70		8.7×10^{15}	
	CIGS	none	25	7	7	36	2.1×10^{15}	−19
		RbF		25	28		1.0×10^{15}	
	ACIS	none	-22	13	13	44	6.7×10^{14}	−7
		KF		64	71		5.2×10^{14}	

discrepancies from 38 to 59 mV remained between total voltage loss and $\tau_{bulk} + N_A$. This indicates that mechanisms which were not included in these voltage change calculations such as interface recombination and/or back contact/band bending were somewhat substantial in these devices. Early-time TRPL fits (τ_1) and front interface recombination velocity (S_{front}) calculations, provided in the Supporting Information section, showed an increase in S_{front} for devices B after PDT. This increase suggests that front interface recombination likely contributed non-negligibly to voltage loss in these devices, although a method for voltage loss quantification of front and back interface contributions is not presently known.

Additional separation of front and back interface recombination in any of the devices would require simulations[22,40] and temperature-dependent *J*–*V* measurements. These techniques extended beyond the scope of this work but could be enacted in future work to extract interface recombination parameters and differentiate between front and back interface contributions. Wolter et al.[24] demonstrated that subband states can also contribute to nonradiative voltage losses, which may be an additional mechanism that impacts the $\Delta V_{OC,bulk} + \Delta V_{OC,NA}$ and $V_{OC,SQ}$–V_{OC} voltage discrepancy.

Figure 3 highlights that independent of the fabrication process or structure, PDTs increase τ_{bulk}. Net acceptor concentration, however, generally decreased in devices with PDT. Therefore, one route to increased voltage is through improved understanding and control of acceptor concentration in PDT devices. A representation such as Figure 3 conveys only relative voltage changes between devices; therefore, it is important to utilize this representation in conjunction with Figure 2. Together, these depictions outline a more well-defined path to targeted voltage increases by providing information about primary and secondary voltage loss categories in devices and submechanisms that generate voltage improvements.

3. Conclusion

Voltage loss identification and reduction are important for increased solar cell power conversion efficiency. For CIGS PV, this includes material improvements (e.g., trap density reduction through PDT processes) and device design advancement (such as absorber GGI grading). To better understand mechanisms that cause voltage losses, we applied consistent characterization methods to CIGS-based solar cells manufactured at three institutions with variations in fabrication, bandgap, absorber structure, PDT, and efficiency.

Two voltage loss categories, radiative and nonradiative (SRH), were delineated through EQE measurements. These categories were further described by parameters that correspond to physical mechanisms: nonideal, subband state absorption, bulk lifetime, and net acceptor concentration.

Total voltage loss (V_{OC} relative to the bandgap-dictated Shockley–Queisser voltage) summed to over 180 mV in each CIGS device, with SRH as the dominant loss mechanism. SRH contributed >75% compared to <25% from radiative voltage loss regardless of the fabrication method, device architecture, or PDT. Generally, PDTs decreased the total voltage loss, driven primarily by SRH loss reduction, and assisted in some cases by reduced radiative losses.

Bulk lifetime was the most significant predictor of SRH voltage changes after PDT. Determined by fits to voltage-biased TRPL data, τ_{bulk} increased after PDT with up to 75 mV of predicted voltage improvement. There was variation in the effect of acceptor carrier concentration on voltage in untreated and PDT samples; most devices demonstrated smaller N_A and voltage reduction after PDT. This highlights a path to further voltage improvements via maintenance or increases in N_A with PDT. The role of interface recombination appeared to vary between devices; future work could include TRPL simulations and temperature-dependent *J*–*V* measurements to separate front and back interface mechanisms. Thus, this work demonstrates that a multi-pronged approach to PV voltage loss analysis is necessary to understand voltage loss mechanisms and pathways to improvement.

4. Experimental Section

Device Fabrication: Devices were provided by three institutions, labeled "A", "B", and "C". Each device was described by its PDT: untreated (no PDT) and RbF from institution A; untreated (no PDT), RbF + S,

© 2023 The Authors. Solar RRL published by Wiley-VCH GmbH

and RbF + In+S from institution B; and $CuInSe_2$ (CIS), CIS RbF, CIGS, CIGS RbF, (Ag,Cu)$InSe_2$ (ACIS), and ACIS KF from institution C.

A Devices: Fabrication: A devices had a Mo-coated soda-lime glass/CIGS/CdS/i-ZnO/ZnO:Al structure described fully in the study of Kanevce et al.[41] The 2.0–2.5 μm CIGS absorber was deposited by coevaporation in a five-unit evaporation vacuum system. The first stage consisted of In, Ga, and Se depositions, and the second stage included Cu and Se deposition for a Cu-rich intermediate phase followed by In, Ga, and Se until a final Cu-poor composition was achieved. This created a linear grading profile.[41] Substrate heater temperatures of ≈450 and ≈650 °C were used for units one and two, respectively. The subsequent two units were used for sample cool down and the fifth unit was used for the PDT. The PDT process included a ramp-up of the RbF source temperature for RbF evaporation onto the CIGS.

A 50 nm CdS buffer layer was deposited on the absorber by chemical bath deposition (CBD) followed by an RF-sputtered 80-nm undoped ZnO layer and DC-sputtered 400-nm Al-doped ZnO window layer. Finished device areas were ≈2 mm^2.

B Devices: Fabrication: B devices had a soda-lime glass/Mo/CIGS/CdS/ZnO/ZnO:Al/metallic grid structure. Complete fabrication details are provided by Polyxeni et al.[42] The polycrystalline CIGS absorber was deposited by a three-stage coevaporation process to achieve a notch-graded bandgap. The first stage consisted of In and Ga coevaporation in a Se atmosphere at a substrate temperature of 375 °C. In stage two, Cu was evaporated in a Se atmosphere until the film became Cu-rich. The third stage consisted of In and Ga coevaporation in a Se atmosphere until the film turned Cu-poor. Stages two and three were performed at a substrate temperature of 575 °C. PDT was enacted in a separate coevaporation vacuum system with a substrate temperature of 350 °C. The RbF + S device received 15 nm of RbF evaporated (3 nm min^{-1}) in S excess (120 nm min^{-1}). The RbF + In+S was treated simultaneously with 15 nm of RbF (3 nm min^{-1}) and 20 nm of In (4 nm min^{-1}) in S excess.

A rinse in an aqueous ammonia solution (1 mol L^{-1}) was used to remove fluoride phases from the surface. CdS was deposited on all devices by CBD using 22 mL ammonia (1 mol L^{-1}), 6 mL thiourea (9.5×10^{-2} mol L^{-1}), and 6 mL cadmium acetate dihydrate (2.6×10^{-3} mol L^{-1}). The CBD process was 360 s for the PDT devices and 420 s for the untreated device. The ZnO/ZnO:Al bilayer was RF-sputtered and electron beam evaporation was used to deposit the metallic grids through a shadow mask for device areas of 0.5 cm^2.

C Devices: Fabrication: C devices had a soda-lime glass/Mo/CI(Ga,Ag)Se/CdS/i-ZnO/ITO/metallic grid structure (see[43,44] for full process details). The ≈2 μm CIS absorber and its Ga and Ag alloys were fabricated in a three-stage coevaporation system. In and Ga (when used) were deposited in the first stage, Cu and Ag (when used) during the second stage, and In and Ga (when used) again during the third stage. A constant Se flux was employed throughout the evaporation with an overpressure maintained at a molar flux rate of greater than six times the total of all metals. Substrate temperatures were 350 °C for the first stage, and 580 °C for both the second and third stages. For PDT samples substrates were cooled to 350 °C in the same system while the alkali-fluoride source ramped to evaporation temperature. The samples were exposed to alkali-fluoride flux for 7.5 min. The Se flux used during absorber growth was kept constant during PDT.

A 50 nm CdS layer was deposited by CBD after the *CIS*-based absorber, followed by a RF sputter-deposited 50 nm i-ZnO layer. Finally, a 150 nm ITO layer was deposited, and Ni-Al grids were subsequently deposited by electron beam deposition. Devices were delineated by mechanical scribing for cell areas of 1.0 cm^2.

Device Characterization: Current density-voltage (J–V) data were measured at standard test conditions: simulated 1-sun AM 1.5G illumination, room temperature, and four-point probe contacting such that V_{OC}, short-circuit current density (J_{SC}), fill factor (FF), and efficiency (η) were extracted. A devices were measured with a WACOM Class A (IEC-60 904-9) solar simulator, B devices were measured with an Oriel Xenon lamp with AM1.5 filter and device temperatures maintained at 25 °C by Peltier controls, and C devices were also measured with an Oriel lamp. External quantum efficiency (EQE) spectra were measured between 300 and 1400 nm on an Oriel 200 system with no external illumination or voltage bias applied. Acceptor carrier concentrations were determined using Mott–Schottky analysis of capacitance–voltage (C–V) data.[45] The C–V profiles of devices A and C were measured at room temperature using a Boonton 7200 capacitance meter with a measurement frequency of 1 MHz and voltage biases from −1 to 0 V. C–V profiles of B devices were measured at room temperature using an Agilent 4294 A precision impedance analyzer with a measurement frequency of 40 kHz across a voltage range of −1.0 to +0.5 V. Despite the different measurement frequencies, each capacitance measurement had a Q-factor >5, indicating accurate capacitance measurements across all devices.[45]

Time-resolved photoluminescence (TRPL) was measured with an excitation wavelength of 640 nm and fluence 1.3×10^{12}–1.0×10^{14} photons cm^{-2} $pulse^{-1}$ (60 μm laser beam diameter). TRPL decays were first measured at various injection levels to identify injection-independent ranges (low injection), which were implemented for final measurement and analysis. 0.3-ps pulses and 1.1 MHz repetition rate were used. Time-correlated single photon counting was used for data collection. A voltage bias of −0.5–+1.0 V was applied across the device contacts for voltage-biased TRPL measurements. Single exponential fits of the TRPL tail decays were performed with $t > 3$ ns and are provided in the applicable figures.

Supporting Information

Supporting Information is available from the Wiley Online Library or from the author.

Acknowledgements

This work was authored in part by the National Renewable Energy Laboratory, operated by Alliance for Sustainable Energy, LLC, for the U.S. Department of Energy (DOE) under Contract No. DE-AC36-08GO28308. Funding is provided by the U.S. Department of Energy Office of Energy Efficiency and Renewable Energy Solar Energy Technologies Office. The views expressed in the article do not necessarily represent the views of the DOE or the U.S. Government. This article has been contributed to by US Government contractors and their work is in the public domain in the USA. This material is based upon work supported by the U.S. Department of Energy's Office of Energy Efficiency and Renewable Energy (EERE) under the Solar Energy Technology Office (SETO) Award Number DE-EE0008755. The authors acknowledge German Federal Ministry for Economic Affairs and Energy under Project Number 03EE1078 (ODINCIGS). This report was prepared as an account of work sponsored by an agency of the United States Government. Neither the United States Government nor any agency thereof, nor any of their employees, makes any warranty, express or implied, or assumes any legal liability or responsibility for the accuracy, completeness, or usefulness of any information, apparatus, product, or process disclosed, or represents that its use would not infringe privately owned rights. Reference, herein, to any specific commercial product, process, or service by trade name, trademark, manufacturer, or otherwise does not necessarily constitute or imply its endorsement, recommendation, or favoring by the United States Government or any agency thereof. The views and opinions of authors expressed herein do not necessarily state or reflect those of the United States Government or any agency thereof.

Conflict of Interest

The authors declare no conflict of interest.

Data Availability Statement

The data that support the findings of this study are available from the corresponding author upon reasonable request.

© 2023 The Authors. Solar RRL published by Wiley-VCH GmbH

2367198x, 2023, 11, Downloaded from https://onlinelibrary.wiley.com/doi/10.1002/solr.202300075 by National Renewable Energy Lab, Wiley Online Library on [08/06/2023]. See the Terms and Conditions (https://onlinelibrary.wiley.com/terms-and-conditions) on Wiley Online Library for rules of use; OA articles are governed by the applicable Creative Commons License

Keywords

$Cu(In,Ga)Se_2$, nonradiative recombination, solar cells, voltage losses

Received: February 1, 2023
Revised: March 22, 2023
Published online: April 20, 2023

[1] A. Luque, S. Hegedus, *Handbook of Photovoltaic Science and Engineering*, John Wiley & Sons, West Sussex, United Kingdom **2011**.
[2] L. M. Mansfield, R. L. Garris, K. D. Counts, J. R. Sites, C. P. Thompson, W. N. Shafarman, K. Ramanathan, *IEEE J. Photovoltaics* **2016**, *7*, 286.
[3] R. Carron, S. Nishiwaki, T. Feurer, R. Hertwig, E. Avancini, J. Löckinger, S. C. Yang, S. Buecheler, A. N. Tiwari, *Adv. Mater.* **2019**, *9*, 1900408.
[4] A. Colthorpe, *Solar Frontier Achieves CIS Thin-Film Lab Efficiency Record of 23.35%*, PVTech **2019**, https://www.pv-tech.org/solar-frontier-achieves-cis-thin-film-efficiency-record-of-23-35/.
[5] M. A. Contreras, J. Tuttle, A. Gabor, A. Tennant, K. Ramanathan, S. Asher, A. Franz, J. Keane, L. Wang, J. Scofield, in *Proc. 1994 IEEE 1st World Conf. Photovoltaic Energy Conversion-WCPEC (A Joint Conf. PVSC, PVSEC and PSEC)*, IEEE, Piscataway, NJ **1994**, pp. 68–75.
[6] N. E. Gorji, M. D. Perez, U. Reggiani, L. Sandrolini, *Int. J. Eng. Technol.* **2012**, *4*, 573.
[7] M. Gloeckler, J. Sites, *J. Phys. Chem. Solids* **2005**, *66*, 1891.
[8] S. Siebentritt, E. Avancini, M. Bär, J. Bombsch, E. Bourgeois, S. Buecheler, R. Carron, C. Castro, S. Duguay, R. Félix, *Adv. Mater.* **2020**, *10*, 1903752.
[9] D. Rudmann, A. Da Cunha, M. Kaelin, F. Kurdesau, H. Zogg, A. Tiwari, G. Bilger, *Appl. Phys. Lett.* **2004**, *84*, 1129.
[10] A. Chirilă, P. Reinhard, F. Pianezzi, P. Bloesch, A. R. Uhl, C. Fella, L. Kranz, D. Keller, C. Gretener, H. Hagendorfer, *Nat. Mater.* **2013**, *12*, 1107.
[11] P. Jackson, R. Wuerz, D. Hariskos, E. Lotter, W. Witte, M. Powalla, *Phys. Status Solidi RRL* **2016**, *10*, 583.
[12] T. Kato, J.-L. Wu, Y. Hirai, H. Sugimoto, V. Bermudez, *IEEE J. Photovoltaics* **2018**, *9*, 325.
[13] S. A. Jensen, S. Glynn, A. Kanevce, P. Dippo, J. V. Li, D. H. Levi, D. Kuciauskas, *J. Appl. Phys.* **2016**, *120*, 063106.
[14] R. Scheer, H.-W. Schock, *Chalcogenide Photovoltaics: Physics, Technologies, and Thin Film Devices*, John Wiley & Sons, Weinheim, Germany **2011**.
[15] T. Dullweber, O. Lundberg, J. Malmström, M. Bodegård, L. Stolt, U. Rau, H.-W. Schock, J. H. Werner, *Thin Solid Films* **2001**, *387*, 11.
[16] S. C. Yang, M. Ochoa, R. Hertwig, A. Aribia, A. N. Tiwari, R. Carron, *Prog. Photovoltaics: Res. Appl.* **2021**, *29*, 630.
[17] M. Contreras, L. Mansfield, B. Egaas, J. Li, M. Romero, R. Noufi, E. Rudiger-Voigt, W. Mannstadt, *Prog. Photovoltaics: Res. Appl.* **2012**, *20*, 843.
[18] P. T. Erslev, J. Lee, G. M. Hanket, W. N. Shafarman, J. D. Cohen, *Thin Solid Films* **2011**, *519*, 7296.
[19] W. N. Shafarman, R. Klenk, B. E. McCandless, *J. Appl. Phys.* **1996**, *79*, 7324.
[20] M. Edoff, T. Jarmar, N. S. Nilsson, E. Wallin, D. Högström, O. Stolt, O. Lundberg, W. Shafarman, L. Stolt, *IEEE J. Photovoltaics* **2017**, *7*, 1789.
[21] A. J. Ferguson, R. Farshchi, P. K. Paul, P. Dippo, J. Bailey, D. Poplavskyy, A. Khanam, F. Tuomisto, A. R. Arehart, D. Kuciauskas, *J. Appl. Phys.* **2020**, *127*, 215702.
[22] A. M. Bothwell, S. Li, R. Farshchi, M. F. Miller, J. Wands, C. L. Perkins, A. Rockett, A. R. Arehart, D. Kuciauskas, *Sol. RRL* **2022**, *6*, 2200230.
[23] S. Siebentritt, *Sol. Energy Mater. Sol. Cells* **2011**, *95*, 1471.
[24] M. H. Wolter, R. Carron, E. Avancini, B. Bissig, T. P. Weiss, S. Nishiwaki, T. Feurer, S. Buecheler, P. Jackson, W. Witte, *Prog. Photovoltaics: Res. Appl.* **2022**, *30*, 702.
[25] T. Kirchartz, U. Rau, *Adv. Mater.* **2018**, *8*, 1703385.
[26] W. Shockley, H. J. Queisser, *J. Appl. Phys.* **1961**, *32*, 510.
[27] U. Rau, B. Blank, T. C. Müller, T. Kirchartz, *Phys. Rev. Appl.* **2017**, *7*, 044016.
[28] W. Ruppel, P. Wurfel, *IEEE Trans. Electron Devices* **1980**, *27*, 877.
[29] U. Rau, *Phys. Rev. B* **2007**, *76*, 085303.
[30] K. Puech, S. Zott, K. Leo, M. Ruckh, H. W. Schock, *Appl. Phys. Lett.* **1996**, *69*, 3375.
[31] E. Spaans, J. de Wild, T. Savenije, B. Vermang, *J. Appl. Phys.* **2021**, *130*, 123103.
[32] M. Maiberg, C. Spindler, E. Jarzembowski, R. Scheer, *Thin Solid Films* **2015**, *582*, 379.
[33] P. M. Jundt, D. Kuciauskas, J. R. Sites, *IEEE J. Photovoltaics* **2021**, *12*, 501.
[34] S. Paul, R. Lopez, M. D. Mia, C. H. Swartz, J. V. Li, in *2017 IEEE 44th Photovoltaic Specialist Conf. (PVSC)*, IEEE, Piscataway, NJ **2017**, pp. 2749–2754.
[35] J. Wands, A. Kanevce, A. Bothwell, M. F. Miller, S. Paetel, A. R. Arehart, A. Rockett, *IEEE J. Photovoltaics* **2022**, *12*, 1400.
[36] F. Pianezzi, P. Reinhard, A. Chirilă, B. Bissig, S. Nishiwaki, S. Buecheler, A. N. Tiwari, *Phys. Chem. Chem. Phys.* **2014**, *16*, 8843.
[37] I. Khatri, H. Fukai, H. Yamaguchi, M. Sugiyama, T. Nakada, *Sol. Energy Mater. Sol. Cells* **2016**, *155*, 280.
[38] I. Khatri, J. Matsuura, M. Sugiyama, T. Nakada, *Prog. Photovoltaics: Res. Appl.* **2019**, *27*, 22.
[39] T. Lepetit, *Influence of KF Post Deposition Treatment on the Polycrystalline Cu(In,Ga)Se2/CdS Heterojunction Formation for Photovoltaic Application*, Université de nantes, Nantes, France **2015**.
[40] J. Moseley, D. Krasikov, C. Lee, D. Kuciauskas, *J. Appl. Phys.* **2021**, *130*, 163105.
[41] A. Kanevce, S. Paetel, D. Hariskos, T. M. Friedlmeier, *EPJ Photovoltaics* **2020**, *11*, 8.
[42] P. Tsoulka, A. Crossay, L. Arzel, S. Harel, N. Barreau, *Prog. Photovoltaics: Res. Appl.* **2022**, *30*, 835.
[43] N. Valdes, J. Lee, W. Shafarman, *Sol. Energy Mater. Sol. Cells* **2019**, *195*, 155.
[44] L. Chen, J. Lee, W. N. Shafarman, *IEEE J. Photovoltaics* **2013**, *4*, 447.
[45] D. Schroeder, *Semiconductor Material and Device Characterization*, Vol. 2, John Wile, New York, NY **1998**.

© 2023 The Authors. Solar RRL published by Wiley-VCH GmbH

2367198x, 2023, 11, Downloaded from https://onlinelibrary.wiley.com/doi/10.1002/solr.202300075 by National Renewable Energy Lab, Wiley Online Library on [08/06/2023]. See the Terms and Conditions (https://onlinelibrary.wiley.com/terms-and-conditions) on Wiley Online Library for rules of use; OA articles are governed by the applicable Creative Commons License